Journal of Atmospheric and Solar–Terrestrial Physics 266 (2025) 106394

Contents lists available at ScienceDirect

Journal of Atmospheric and Solar-Terrestrial Physics

journal homepage: www.elsevier.com/locate/jastp

Research Paper

Observation and simulation studies of ionospheric F-region in the South American and Antarctic sectors in the intense geomagnetic storm of August 2018

A.J. de Abreu [a,b,*], E. Correia [a,c], O.F. Jonah [d], K. Venkatesh [e], E.G. Thomas [f], R. de Jesus [a], M. Roberto [b,1], J.R. Abalde [b], P.R. Fagundes [g]

[a] Instituto Nacional de Pesquisas Espaciais (INPE), São José dos Campos, SP, Brazil
[b] Instituto Tecnológico de Aeronáutica (ITA), Divisão de Ciências Fundamentais, São José dos Campos, SP, Brazil
[c] Centro de Rádio Astronomia e Astrofísica Mackenzie, Universidade Presbiteriana Mackenzie, SP, Brazil
[d] SRI International Geospace Group, Menlo Park, Ca, USA
[e] National Atmospheric Research Laboratory (NARL), Gadanki, India
[f] Thayer School of Engineering, Dartmouth College, Hanover, NH, USA
[g] Laboratório de Física e Astronomia, Universidade do Vale do Paraíba (UNIVAP), São José Dos Campos, SP, Brazil

ARTICLE INFO

Handling editor: Dora Pancheva

ABSTRACT

In this investigation, we present and discuss the ionospheric F region observations in the equatorial, low-, mid-, and near high-latitude regions in the South American and Antarctic sectors during the intense geomagnetic storm that occurred on 25–27 August 2018. The geomagnetic storm reached a minimum Dst of −175 nT at ~0700 UT on 26 August. We present the variations of vertical total electron content (VTEC) from a chain of almost 200 GPS stations, covering the South American and Antarctic sectors. A comparison with model simulations from the Thermosphere Ionosphere Electrodynamics General Circulation Model (TIE-GCM) is realized. The results obtained show that during the main phase of the storm, a southward Bz component of the interplanetary magnetic field (IMF) and an eastward prompt penetration electric field (PPEF) can be observed, but they had no significant impact on the ionospheric plasma. A long recovery phase a predominance of positive phase is observed during daytime. The observations show the effects of an unusual case of multiple PPEF, occurred on 26 August, and effects of thermospheric winds disturbances, occurred on 27 August, resulting in increased VTEC values on both days. The TIE-GCM model reproduces the VTEC increases during the main and recovery phases from mid-latitudes to the equatorial region, but it underestimates the observed values near high-latitudes.

1. Introduction

Geomagnetic storms are important space weather events that have been studied for over 50 years by the scientific community (Willis, 1964; Gonzalez et al., 1990; Zolotukhina et al., 2017, and references therein). Geomagnetic storms are disturbances of the geomagnetic field that can cause various damages in technological systems, including problems in telecommunication applications such as disturbing the global navigation satellite system (GNSS) (Buonsanto, 1999; Boteler et al., 1998). Geomagnetic storms usually start with a sudden storm commencement (SSC), which indicates the arrival of an interplanetary shock structure (the initial phase). Following the SSC, the interplanetary magnetic field (IMF), Bz component, turns to the South and the ring current builds up (main phase), and then returns to normal conditions (recovery phase). During the main phase, the Bz component of the IMF interconnects with the lines of the geomagnetic field, leading to a large amount of energy input in high-latitude regions where the geomagnetic field is nearly vertical. During the recovery phase, geomagnetic activity decreases and the energy input is minimized (Akasofu, 1981; Gonzalez et al., 1990).

The response of the ionospheric F region during a geomagnetic storm is commonly referred to as an ionospheric storm, which has been studied for decades at different latitudes and longitudes from observations and theoretical models (Klimenko et al., 2011; Sahai et al., 2007, de Jesus et al., 2013, Venkatesh et al., 2017; de Abreu et al., 2017, and 2023;

* Corresponding author. Instituto Nacional de Pesquisas Espaciais (INPE), São José dos Campos, SP, Brazil.
E-mail address: abreu.alessandro@gmail.com (A.J. de Abreu).
[1] Dr. Marisa Roberto – in memoriam.

https://doi.org/10.1016/j.jastp.2024.106394
Received 24 May 2024; Received in revised form 30 October 2024; Accepted 5 December 2024
Available online 7 December 2024

Fagundes et al., 2023, and references therein). However, complete understanding of ionospheric behaviour during geomagnetic storms remains one of the main issues addressed in the study of ionospheric physics. Ionospheric storms have often been categorized by their positive and negative phases. A positive phase results in an increase in electron density relative to the average of values obtained in geomagnetically quiet periods. A negative phase results in a decrease in electron density with respect to quiet time (Prölss, 1993). It is already well known that the response of the ionospheric F region during a geomagnetic storm varies significantly with latitude (Foster and Rideout, 2005), season (Zou et al., 2014), local time (Fuller-Rowell et al., 1996) and also by the influence of winds and electric fields (Richmond and Lu, 2000).

There are two main categories of storm-time electric fields. The first category is that generated by prompt penetration towards the magnetic equator of the magnetospheric electric fields in high-latitude regions. These fields occur on fairly short timescales (~few hours) just after the onset of the main phase of the geomagnetic storm. Prompt penetration is generated due to undershielding conditions, when the ring current becomes builds up and the R2 field aligned currents becomes weaker. When the ring current weakens during the recovery phase, overshielding occurs. (Richmond and Kamide, 1988; Veenadhari et al., 2010; Kikuchi et al., 2022). The second main category is related to the electric fields produced by the disturbed dynamo generated by the change in global wind circulation due to particle precipitation in the auroral region, which move to low-latitudes (Maruyama et al., 2005; Klimenko et al., 2011). This second category of electric fields is typically observed on timescales of several hours after the onset of the storm main phase. Both prompt penetration and disturbed dynamo electric fields can produce drastic changes in the ionosphere at equatorial, low-, mid-, and high-latitudes, such as an increase or decrease in the height of the F region and changes in the composition of neutral constituents (Younas et al., 2021; Chingarandi et al., 2023). Thus, more studies involving the magnetosphere and ionosphere interaction during geomagnetic storms are needed using observations and simulations.

During the solar minimum period of the solar cycle 24, an intense geomagnetic storm occurred on the days 25–27 August 2018. This storm has been studied by several researchers in different latitudes/longitudes around the world (Ren et al., 2020; Akala et al., 2021; Spogli et al., 2021; Mansilla and Zossi, 2022). Using multiple observations, as aurora, high-latitude convection, potential patterns, and total electron content (TEC) maps, Ren et al. (2020) found that the high-speed solar wind (HSS) was effective in modulating the ionosphere during the storm of August 26, 2018. Akala et al. (2021) investigated the solar origins of the August 26, 2018 geomagnetic storm as well as the responses of the equatorial to low-latitude ionosphere using multi-instrument. The results showed the a storm was driven by an aggregation of weak coronal mass ejection (CME) transientes and corotating interaction regions/high speed streams (CIR/HSSs). Their results also showed a clear hemispherical asymmetry, with higher TEC in the Northern Hemisphere. The major factors of the ionospheric response during this storm were the local time of the storm onset, local time of minimum SYM-H, and changes in thermospheric O/N_2 ratio. Spogli et al. (2021), using China Seismo-Electromagnetic Satellite (CSES-01) and ground-based observations (ionosondes, magnetometers, and GPS-TEC), investigated the ionospheric response at lower and mid-latitudes over Brazil during the August 26, 2018 geomagnetic storm. They showed that the increased thermospheric circulation driven by the storm has an impact on the EEJ during recovery phase. They also showed signatures of equatorial ionospheric anomaly crests' formation and modification during daytime coupled with the positive ionospheric storm effects at mid-latitudes. Mansilla and Zossi (2022) using ionospheric F region critical frequency (foF2), height (hmF2), and TEC in the South American sector, showed that during the main phase of the intense geomagnetic storm of August 26, 2018, there was a decrease in foF2 at near equatorial and low-latitudes and a small increase at mid-latitudes. During the recovery phase, there was a positive phase in foF2 and TEC at all latitudes possibly due an enhanced ratio of thermosphere neutral composition O/N_2.

The main objective of this paper is to broaden the understanding of the response of the ionospheric F region during the geomagnetic storm of 25–27 August 2018. The focus is to analyze the South American and Antarctic sectors, which have not yet been explored during this storm, using GPS-TEC observations and comparison with the Thermosphere Ionosphere Electrodynamics General Circulation Model (TIE-GCM). Modern society is dependent on new communication technologies, ranging from radio broadcasting to the most complex satellite navigation systems, which are based on electromagnetic wave technology. Thus, the present study is very significant for a better understanding of the physical phenomena on the South American and Antarctic sectors. Because high-latitudes, still little explored, which are the gateway for ionospheric disturbances that propagate to lower latitudes due to the field lines are almost vertical to the Earth's surface. In this way, this study helps to improve space weather forecast models and mitigate the effects on technological systems caused by geomagnetic storms.

2. Data and methodology

2.1. GPS-TEC observations

The Global Positioning System (GPS) data were obtained from Receiver Independent Exchange (RINEX) files for almost 200 stations over the South American and Antarctic sectors. The GPS data belong to the "Rede Brasileira de Monitoramento Contínuo (RBMC)", operated by the "Instituto Brasileiro de Geografia e Estatística (IBGE) (https://www.ibge.gov.br), "Red Argentina de Monitoreo Satelital Continuo (RAMSAC)" (https://www.ign.gob.ar/), and International GNSS Service (IGS) (https://network.igs.org/) networks. Fig. 1 shows the locations of the GPS sites from the three data networks used in the present study.

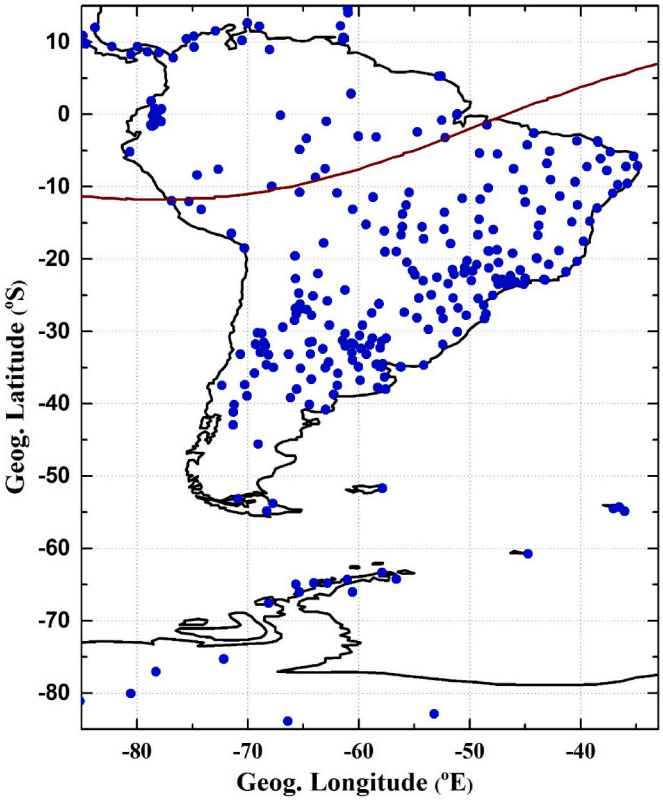

Fig. 1. Map of South American and Antarctic sectors showing the locations of GPS stations used in the presente study. The geographic longitude and latitude are shown in the map.

The GPS RINEX data were used to obtain the slant electron content (STEC), in units of TEC (1 TECU = 10^{16} electrons/m^2) according to the relation (Klobuchar, 1996; Pandit et al., 2021):

$$STEC = \frac{1}{40.3}\left(\frac{f_1^2 f_2^2}{f_2^2 - f_1^2}\right)(P_1 - P_2) \quad (1)$$

where P1 and P2 are the pseudo-ranges for frequencies f1 (1575.42 MHz) and f2 (1227.60 MHz), respectively.

The STEC is the integrated TEC along the line from the GPS satellite to the receiver, which is converted to vertical TEC (VTEC):

$$VTEC = (STEC - B_s - B_u)\left(\sqrt{1 - \left(\frac{(R_e \times \cos\varepsilon)^2}{(R_e + h)^2}\right)}\right) \quad (2)$$

where Bs and Bu are the satellite and receiver instrumental biases, respetively; ε is the elevation angle of the satellite; Re (6371 km) is the mean radius of the Earth; and h is the ionospheric pierce point altitude. The VTEC used in this work is calculated using the software developed by Seemala and Valladares (2011).

The percentage (%) of error between TIE-GCM TEC and GPS TEC is calculated by:

$$\%\ error = \frac{TIE - GCM\ VTEC - GPS\ VTEC}{GPS\ VTEC} * 100 \quad (3)$$

The global GPS-TEC maps from the Madrigal database were obtained from http://madrigal.haystack.mit.edu/madrigal/. For more details on calculating the TEC maps, see Rideout and Coster (2006) and Vierinen et al. (2016).

2.2. TIE-GCM model

The Thermosphere-Ionosphere-Electrodynamics General Circulation Model (TIE-GCM) model (Roble and Ridley, 1987) is a comprehensive, three-dimensional, nonlinear representation of the coupled thermosphere and ionosphere, which includes a self consistent electric field solution. The model has a public Runs-on-Request system directly on the website https://ccmc.gsfc.nasa.gov/models/TIE-GCM~2.0. The inputs are: model version, time interval, F10.7, Kp, and Bx, By, Bz, and Vx parameters. The model encompasses the physical and chemical processes relevant to the upper stratosphere and self-consistently solves the continuity, momentum, and energy equations involving the coupling of the ionosphere-thermosphere system. The model is built on a fixed spherical coordinate system relative to Earth's rotation with horizontal axes of latitude and longitude and a vertical axis of pressure surfaces. The model calculates the global distributions of the neutral gas temperature and winds, the constant pressure surface height and the number densities of the major constituents, i. e, O_2, N_2, and O, including minor neutral constituents. TIE-GCM includes boundaries of approximately 97 and 500 km and a resolution of 5° × 5° in latitude and longitude, and the results provide important information about thermospheric and ionospheric dynamics that are useful when discussing potential mechanisms for directly observed variations in TEC (Jonah et al., 2020).

2.3. CTIPe model

The Coupled Thermosphere Ionosphere Plasmasphere electrodynamics (CTIPe) model (Fuller-Rowell et al., 1987) simulates the vector of wind, temperature and density of the thermosphere at high-, mid-, and low-latitudes across the globe, numerically solving the momentum, energy and continuity equations. The model has a public Runs-on-Request system directly on the website https://ccmc.gsfc.nasa.gov/models/CTIPe~4.1. The inputs are: time interval, B, IMF, clock angle, Dipole Tilt, Vp, Np, and HP index parameters. The model shows the global distribution of the three main species (atomic oxygen, molecular nitrogen and molecular oxygen). In this way, it is possible to analyze the distribution of the O/N_2 rate at any latitude and its relationship with VTEC variations.

2.4. Interplanetary and geomagnetic parameters

The interplanetary magnetic field Bz component (IMF-Bz) in geocentric solar magnetospheric (GSM) coordinates, solar wind proton bulk velocity (Vp), and solar wind ion density (Np) were obtained from the Advanced Composition Explorer (ACE) satellite from the website http://www.srl.caltech.edu/ace/. GSM coordinates can be defined by three axes. The x-axis is the point from the center of the Earth to the Sun. The y-axis is perpendicular to both the magnetic dipole axis and the Earth-Sun line, and positive towards dusk. The z-axis, which consequently is in the plane containing both the Earth-Sun line and the dipole axis (Laundal and Richmond, 2016).

The polar cap magnetic index localized in the northern (PCN) and southern (PCS) near-pole regions at every 1-min interval were obtained from the website http://www.pcindex.org. The planetary geomagnetic (Kp) index indicating storm intensity in 3-hourly values were obtained from the website http://ftp.gwdg.de./pub/geophys/kp-ap/tab/. The disturbance storm time (Dst) index associated with the hourly ring current values were obtained from the world data centre (WDC) in the website http://wdc.kugi.kyoto-u.ac.jp. The variations of prompt penetration of electric field (PPEF) model were obtained from the website https://geomag.colorado.edu/real-time-model-of-the-ionospheric-electric-fields.

3. Results

3.1. Variations of the interplanetary and geomagnetic parameters

Fig. 2 shows the variations of the total interplanetary magnetic field (IMF-B), z component of IMF-Bz, solar wind proton velocity (Vp), solar wind ion density (Np), geomagnetic polar indices northern (PCN) and southern (PCS), planetary geomagnetic (Kp), and disturbance storm time (Dst) indices from 25 to August 30, 2018. The vertical dashed lines indicate the main phase onset (MPO) and recovery phase onset (RPO) times. This geomagnetic storm event was classified as the 3rd largest geomagnetic storm of the 24th solar cycle after March 2015 and June 2015 storms. The storm was caused by a non-AR central filament two-step eruption on 20 August, which was accompanied by two consecutive Earth-directed low-speed CMEs, similar to the strong geomagnetic storm that occurred on August 26, 2018 (Chen et al., 2019).

The MPO time is at ~1900 UT on 25 August. The Dst starts decreasing from 12 nT at 1900 UT becoming negative and attaining a minimum value of −175 nT at ~0700 UT on 26 August. During the main phase, the Kp reachs a maximum of 7^- and the PCN and PCS show strong fluctuations, reaching a maximum of around 7.5 mV/m. The intensity of IMF-B increases from −13 nT at ~1715 UT on 25 August to over 18 nT at ~0530 UT on 26 August, when the IMF-Bz turns southward and reaches its lowest value at ~0530 UT. The Vp fluctuates around 350 km/s, whereas the Np increases from 5 cm to 3 on 25 August to 20 cm-3 on 26 August during the main phase.

The RPO time is at ~0700 UT on 26 August. The Dst shows a long period of recovery phase of the storm, which only returns to the quiet level on 29 August. The recovery phase of the storm shows strong variations with Kp reaching a level 6 and the PCN and PCS of ~6 mV/m on 26 and 27 August. The IMF-Bz and Np also shows strong fluctuations on 26 August, and Vp shows an increase in speed reaching ~700 km/s at 2000 UT on 27 August (Fig. 2).

3.2. Latitudinal TEC variations from observations and model simulations

Fig. 3 shows the time variations of VTEC (red lines) obtained at 10 GPS stations over the South American and Antarctic sectors, which are

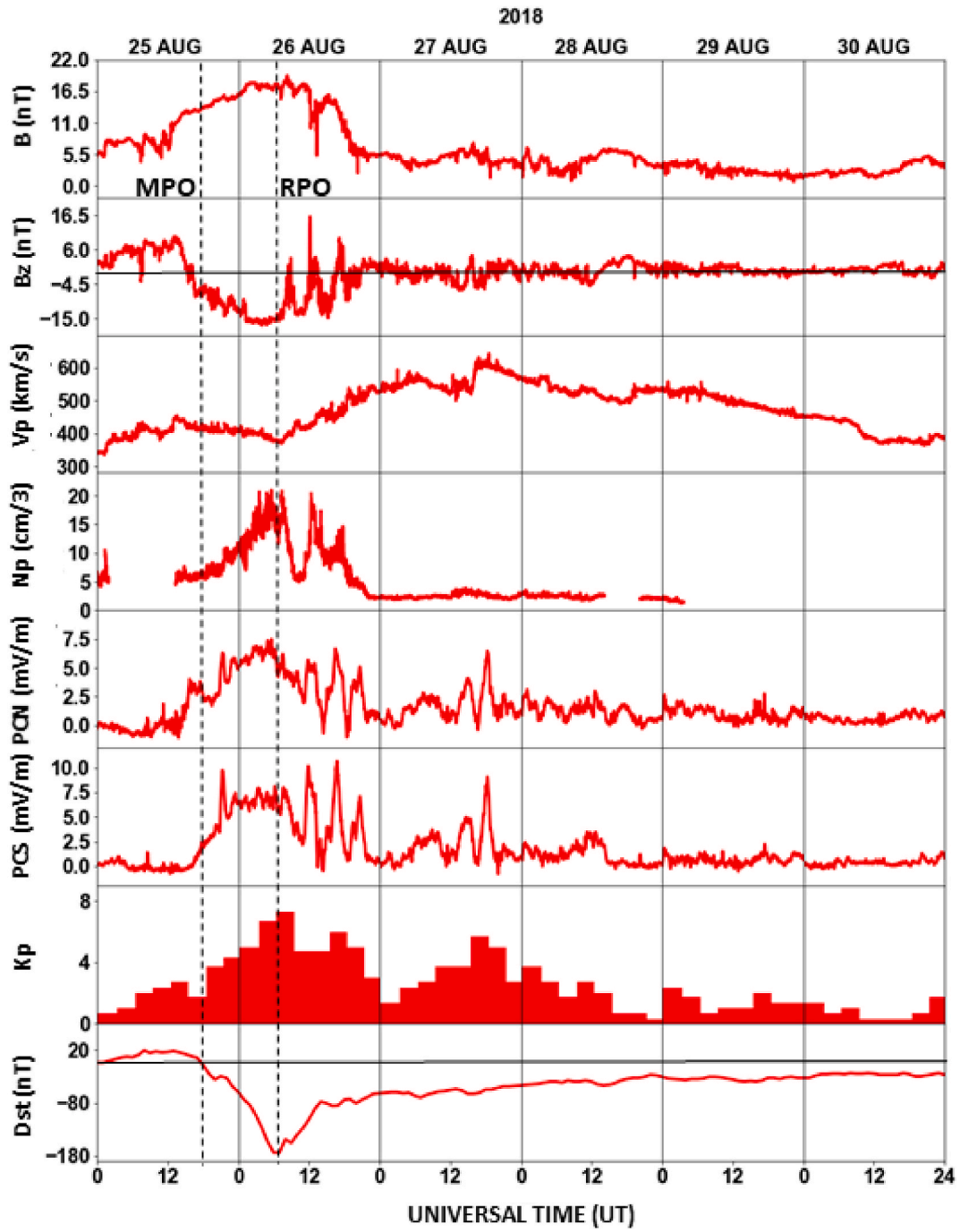

Fig. 2. Variations of the total interplanetary magnetic field (IMF) B, z component of IMF Bz in GSM coordinates, solar wind proton bulk velocity Vp, and solar wind ion density proton Np, obtained from the ACE satellite during the period from 25 to August 30, 2018. Also, the PCN, PCS, Kp, and Dst geomagnetic indices during the same period are presented. The vertical dashed lines indicate the main phase onset (MPO) and recovery phase onset (RPO).

compared with VTEC values obtained with the TIE-GCM model (blue lines) from 25 to August 30, 2018. The gray bands are ±1 standard deviation of the average quiet day's values. The vertical dashed lines indicate the main phase onset (MPO) and recovery phase onset (RPO) times. During the onset and throughout the main phase of the storm, which occurred between 25 (~1900 UT; ~1600 LT) and 26 (~0700 UT; ~0400 LT) August, the VTEC variations are not significant when compared to the geomagnetically quiet period from the equatorial to the mid-latitudes. A weak and short positive phase can be observed at the TOPL and BRAZ stations in the Brazilian sector, NESA and AUTF stations in the Argentinean sector, and OHI2 station in Antarctica. The TIE-GCM model show VTEC values below the observations (storm-day and quiet period) at stations from equator to low-latitudes (SALU to UFPR) and at near high-latitudes (AUTF and OHI2). Therefore, the TIE-GCM is showing negative storm effects at several locations which is not seen in the observations.

The greatest effects of the storm are observed during the long recovery phase, which began after 0700 UT (0400 LT) on 26 August remained evident until the end of 29 August. The most intense effects occur during the first two days of the recovery phase of the storm and gradually lost strength until the third day. A strong diurnal positive phase can be seen on 26 and 27 August at all stations, characterized by an increase in VTEC. The positive phase is greatest in the equatorial and low-latitudes regions and decreases in the mid- and near the high-

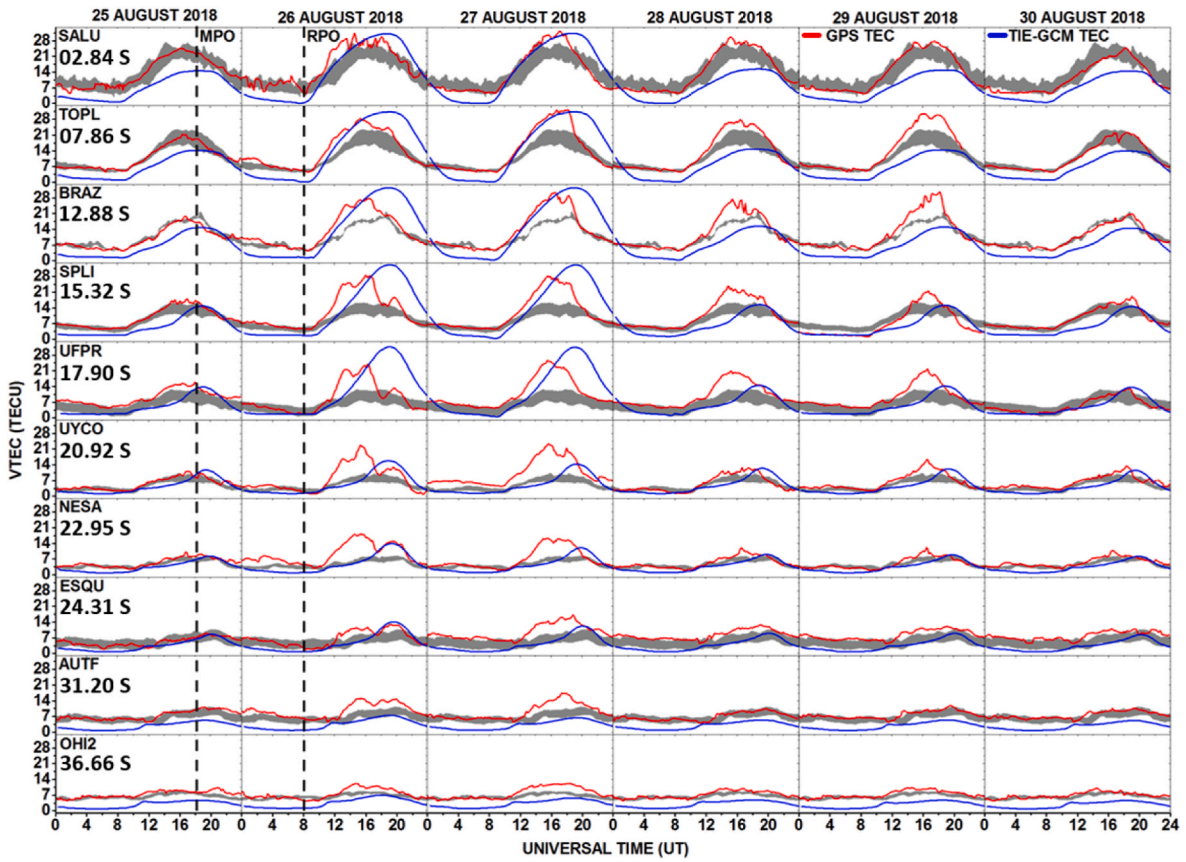

Fig. 3. Variations of the vertical total electron content (VTEC) (red lines) from GPS observations obtained from different satellites at 10 stations over the South American and Antarctic sectors and comparison with TIE-GCM model (blue lines) during the period from 25 to August 30, 2018. The gray bands are ±1 standard deviation of the average quiet day's values. The vertical dashed lines indicate the storm main phase onset (MPO) and recovery phase onset (RPO). The latitude dip is also shown for each station.

latitudes. The positive phase is also observed in the daytime at the end of the recovery phase (days 28 and 29), but now, the effects are more pronounced in the equatorial and low-latitude regions with VTEC gradually decreasing at near high-latitudes, showing no effect at AUTF and OHI2. The VTEC observed on 26 August shows a complex variation suggesting two peaks, one at ~1500 UT (~1200 LT) and other at ~2030 UT (~1730 LT), which are more evident between stations SPLI and ESQU, while at other stations, the VTEC shows only a large maximum involving both peaks. On the other hand, the TIE-GCM VTEC values show a strong positive storm up to ESQU station on this day, with maximum at ~2000 UT (~1700 LT), but extending up to ~2400 UT (~2100 LT), while the GPS-VTEC observations shows the positive phase ending ~2200 UT (~1900 LT).

Fig. 4 shows the VTEC contour plots (4 A) as a function of UT and day from 25 to August 30, 2018 for 10 stations over the South American and Antarctic sectors and comparison with TIE-GCM model (4 B). The results clearly show a strong VTEC during the daytime in the recovery phase of the storm, decreasing as we move towards near higher-latitudes. The same variations occur with the TIE-GCM, agreeing with the results presented in Fig. 3. Observations show strong variations in VTEC until 29 August from the equatorial to low-latitudes regions, decreasing towards near high-latitudes. The same is not predicted by TIE-GCM, which only shows a strong impact until the 27 August.

Fig. 5 shows the percentage (%) error between TIE-GCM and GPS-VTEC from 25 to August 30, 2018 for 10 stations over the South American and Antarctic sectors. The percentage (%) error indicates the discrepancy between observational and modeled VTEC values. The percentage (%) error was scaled to a scale of 0–100 for better understanding. The equatorial (SALU) to low-latitude regions (UFPR) shows a greater deviation when compared with the mid- and near high-latitudes (UYCO to OHI2). During daytime, the TIE-GCM values are lower than GPS-VTEC values from the equatorial to mid-latitudes regions until ~1600 UT (~1300 LT) on 26 and 27 August. After this time, the values are higher until ~2400 UT (~2100 LT). During 26 and 27, the SALU and TOPL stations show deviations of ~10% between 2400 (2100 LT) and 1000 UT (0700 LT) and the other stations up to 1600 UT (1300 LT). After this time, the stations show large deviations above 70% from SALU to UYCO, while the stations from NESA to OHI2 do not show relevant deviations.

In order to better understand the relationship between TIE-GCM and GPS-VTEC values, Fig. 6 shows the scatterplot between them for the period from 25 to 30 August for 10 stations over the South American and Antarctic sectors. Each station is denoted by a color according to the sequence shown on the right of the figure. It is possible to observe a good correlation in stations at mid- and near to high-latitudes between 2400 (2100 LT) and 1000 UT (0700 LT), which corresponds to electron density between 1 and 7 TECU, for all observed days. During the daytime and early evening (from 8 TECU onwards), a large dispersion is observed in the equatorial and low-latitudes regions. The period with the greatest dispersion is during the recovery phase of the storm (26 and 27 August). Overall, the results indicate that the TIE-GCM model reproduced the effects of the geomagnetic storm (showing higher electron density in this period), but not with expected accuracy. The model discrepancies during main and recovery phases of the storm, indicate that the model underestimates the observations, mainly during the daytime.

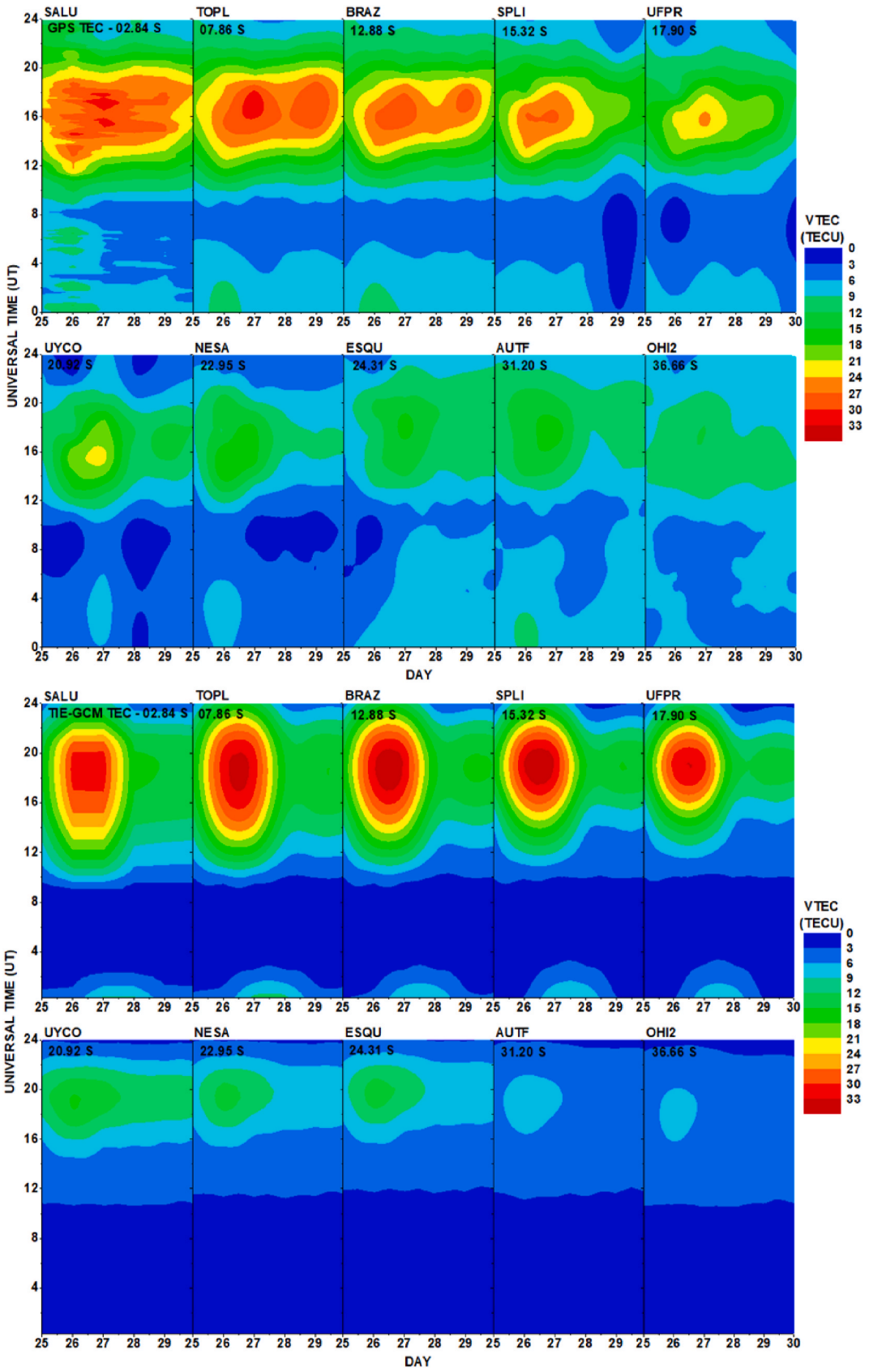

Fig. 4. Variations of the vertical total electron content (VTEC) as a function of UT and day from 25 to August 30, 2018 for 10 stations over the South American and Antarctic sectors and comparison with TIE-GCM model. The latitude dip is also shown for each station.

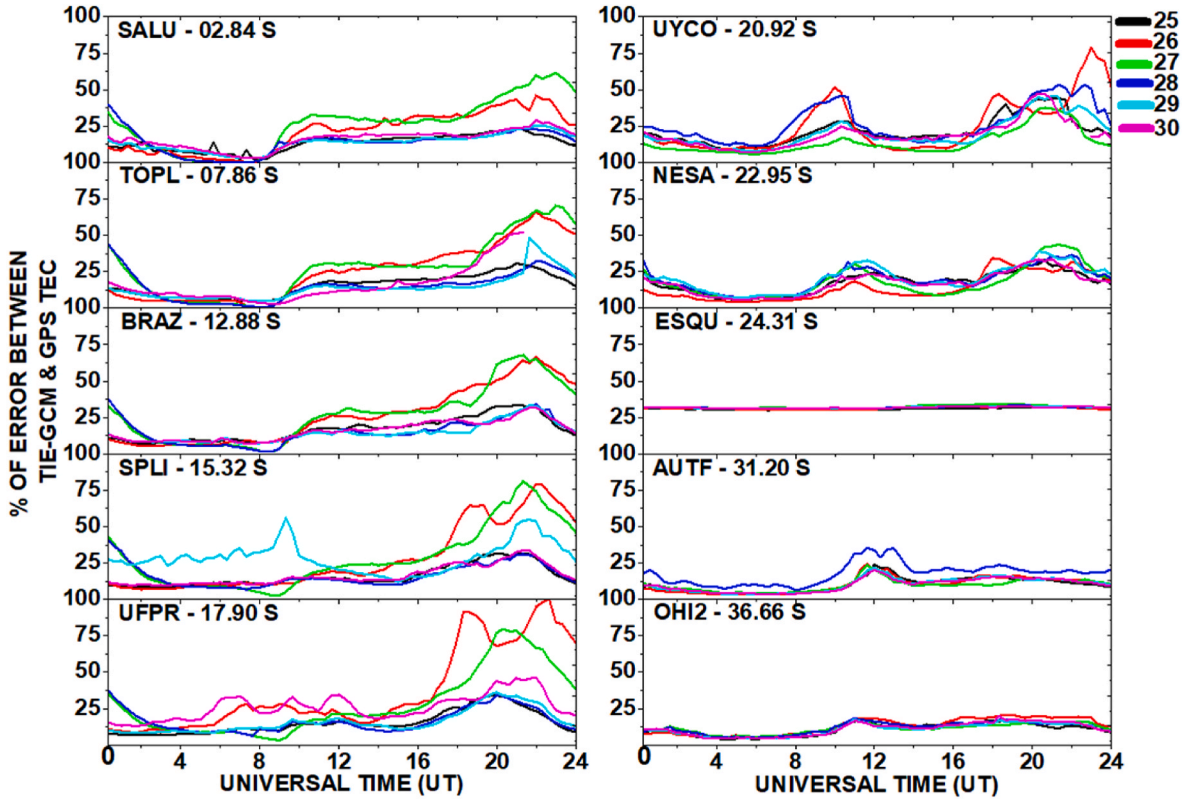

Fig. 5. Percentage (%) error between TIE-GCM TEC and GPS-TEC during the period from 25 to August 30, 2018 for 10 stations over the South American and Antarctic sectors. The latitude dip is also shown for each station.

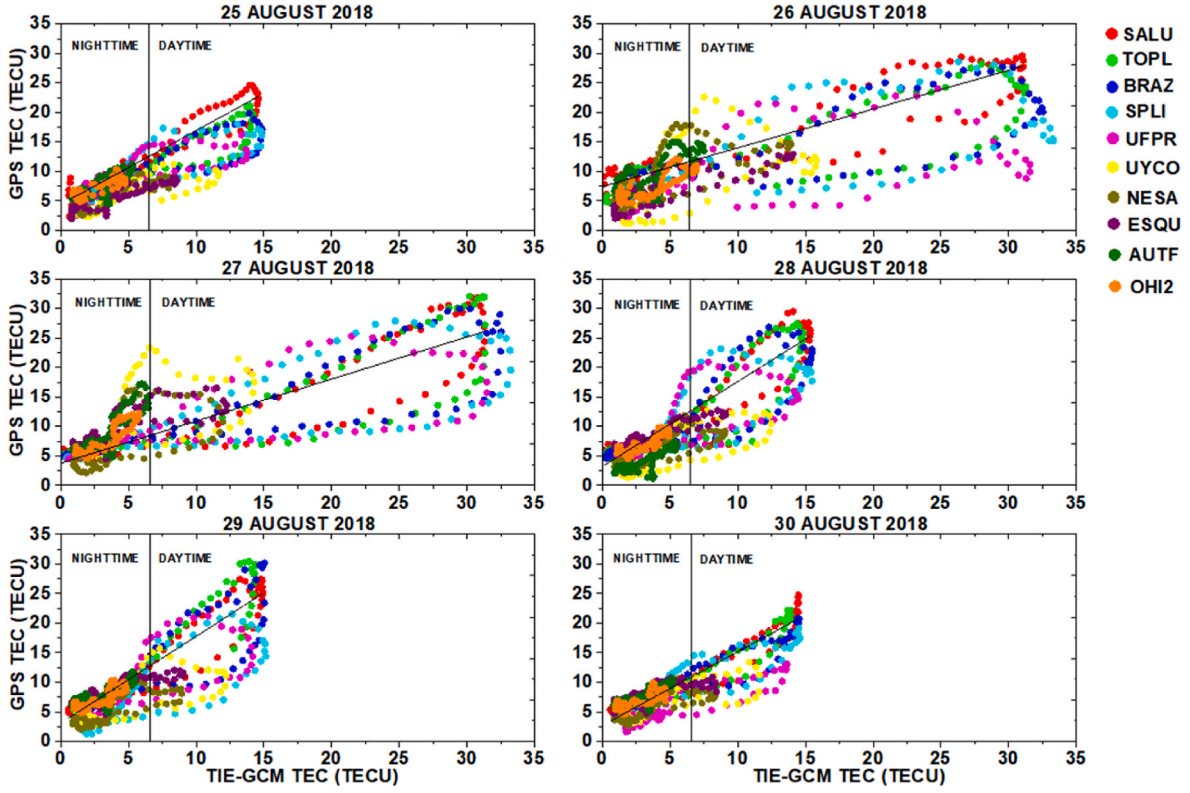

Fig. 6. Scatterplot of the GPS-TEC as a function of the TIE-GCM for the period from 25 to August 30, 2018 for 10 stations over the South American and Antarctic sectors. Each station is denoted by a color according to the sequence shown on the right of the figure.

3.3. General overview of the TEC in the spatial and temporal domains

The dTEC (VTEC – $VTEC_{med}$) maps as a function of geographic longitude and latitude over the South American sector using observations from nearly 150 GPS stations are presented in Fig. 7. The maps are from 25 to August 28, 2018 at 30 min intervals from 0830 to 2000 UT for each day. The maps present a general overview of the dTEC observations during the main and recovery phases of the storm. The

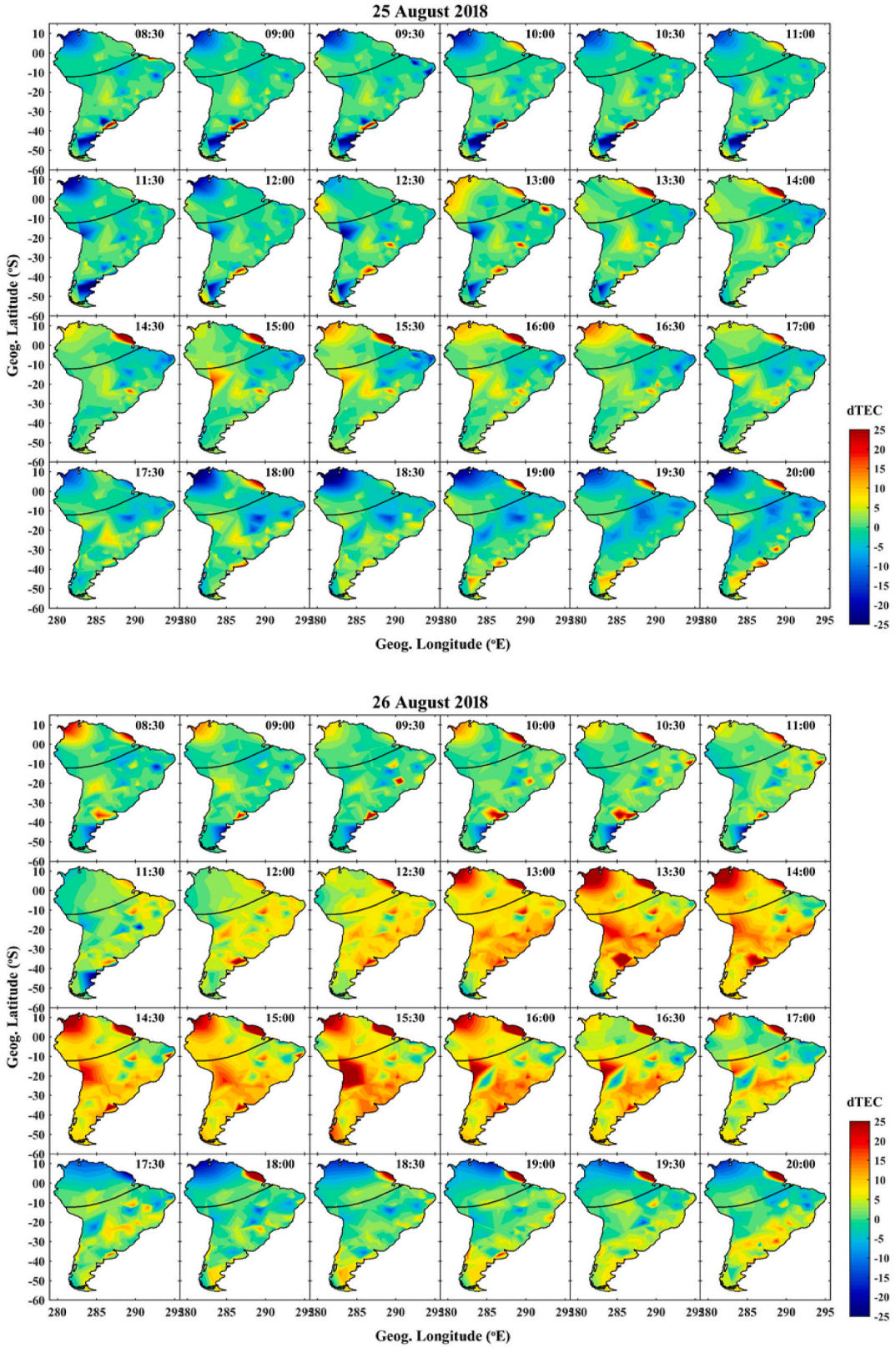

Fig. 7. dTEC (VTEC – $VTEC_{med}$) maps as a function of geographic longitude and latitude over the South American sector with contributions from nearly 150 GPS stations. The maps are from 25 to August 28, 2018 at each 30 min from 0830 to 2000 UT.

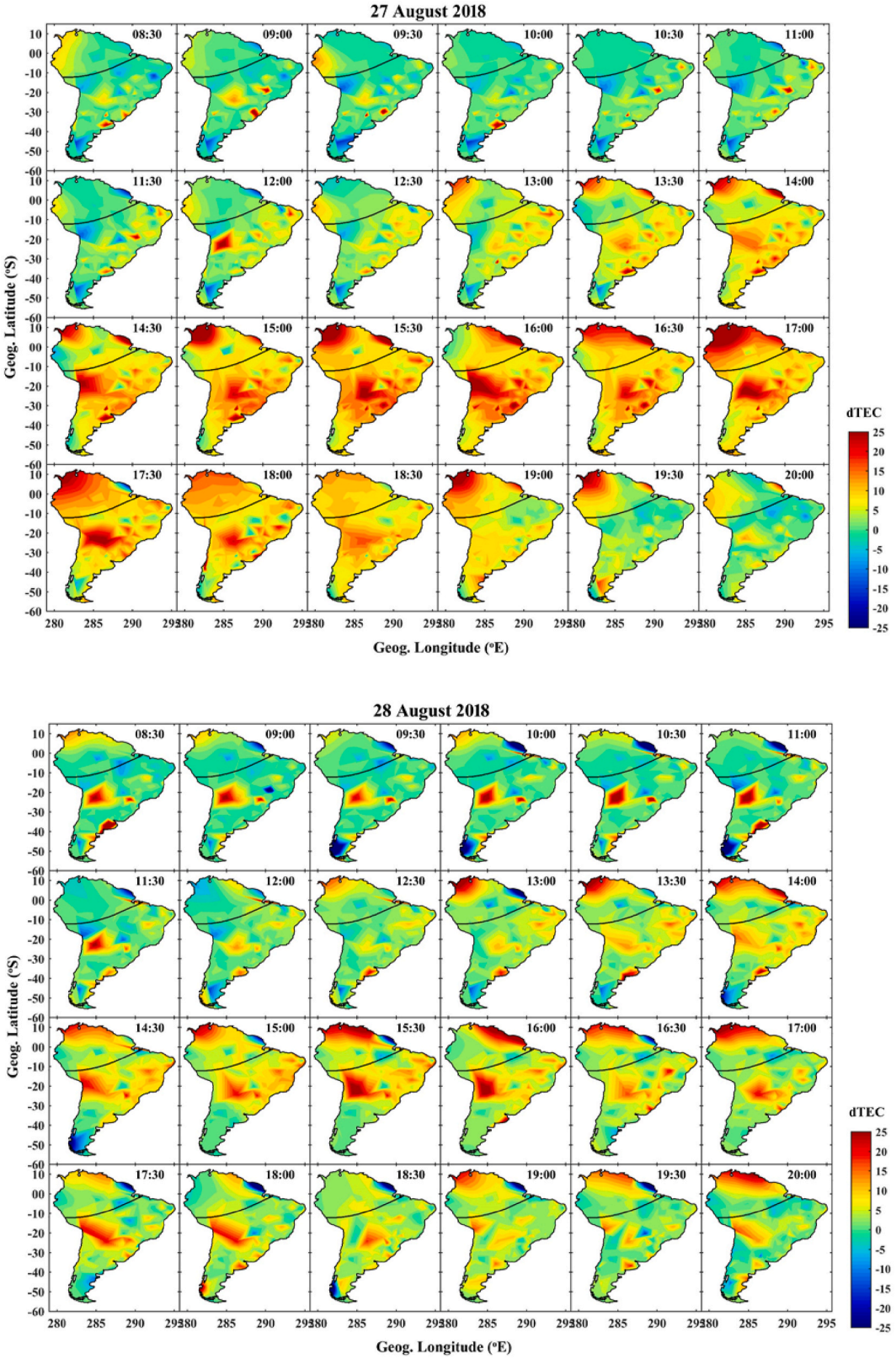

Fig. 7. (*continued*).

maps show weak changes during the main phase that occurred during nighttime in the South American sector, but show strong changes in dTEC from 26 to 28 during recovery phase. An increase in dTEC is clearly observed after RPO (0830 UT) on day 26. Thus, strong variations in dTEC are observed over a large area in this sector. These results indicate a steady increase in the positive phase on 26 August, with highest intensity observed during afternoon time on 26 and 27 August. From day 28 onwards, which corresponds to the end of the recovery phase, there is a decrease in dTEC values, indicating a predominantly weak positive phase. The VTEC (Figs. 3 and 4) and dTEC maps (Fig. 7)

highlight the latitudinal and longitudinal impact of geomagnetic storm over the ionosphere in the South American sector.

Fig. 8 shows TEC maps obtained from the Madrigal database with nearly 200 global GPS stations from 25 to August 28, 2018. This figure shows the development of the storm including higher latitudes in the Antarctic sector, up to low-latitudes, in South America. On day 25, prior to the MPO, the maps show much lower TEC values compared to days 26, 27, and 28. This indicates a strong response from the ionosphere during the storm period. However, the greatest effects occur throughout the day, during the RPO, agreeing with the results in Fig. 7. An interesting characteristic observed is that the TEC increases from north to southwest, with an increase in the TEC further east and then west, as Fig. 7 also suggests. This is clearly observed on day 26 between 1100 UT and 1700 UT. On day 27, the second day of the RPO, it is possible to see this increase in the low- and mid-latitudes in the South American sector.

4. Discussion

The response of the ionospheric F region in the South American and Antarctic sectors during an intense geomagnetic storm that occurred on 25–27 August 2018 is investigated. The different responses of the ionospheric storm are analyzed using GPS-TEC observations and comparison with the TIE-GCM model. Prompt penetration electric fields (PPEF), disturbance dynamo electric fields (DDEF), neutral winds, and consequently composition changes (ratio of O/N_2) are the main physical mechanisms responsible for explaining the ionospheric storm effects (positive and negative phases) during different phases of the geomagnetic storm (Blanc and Richmond, 1980; Danilov and Morozova, 1985;

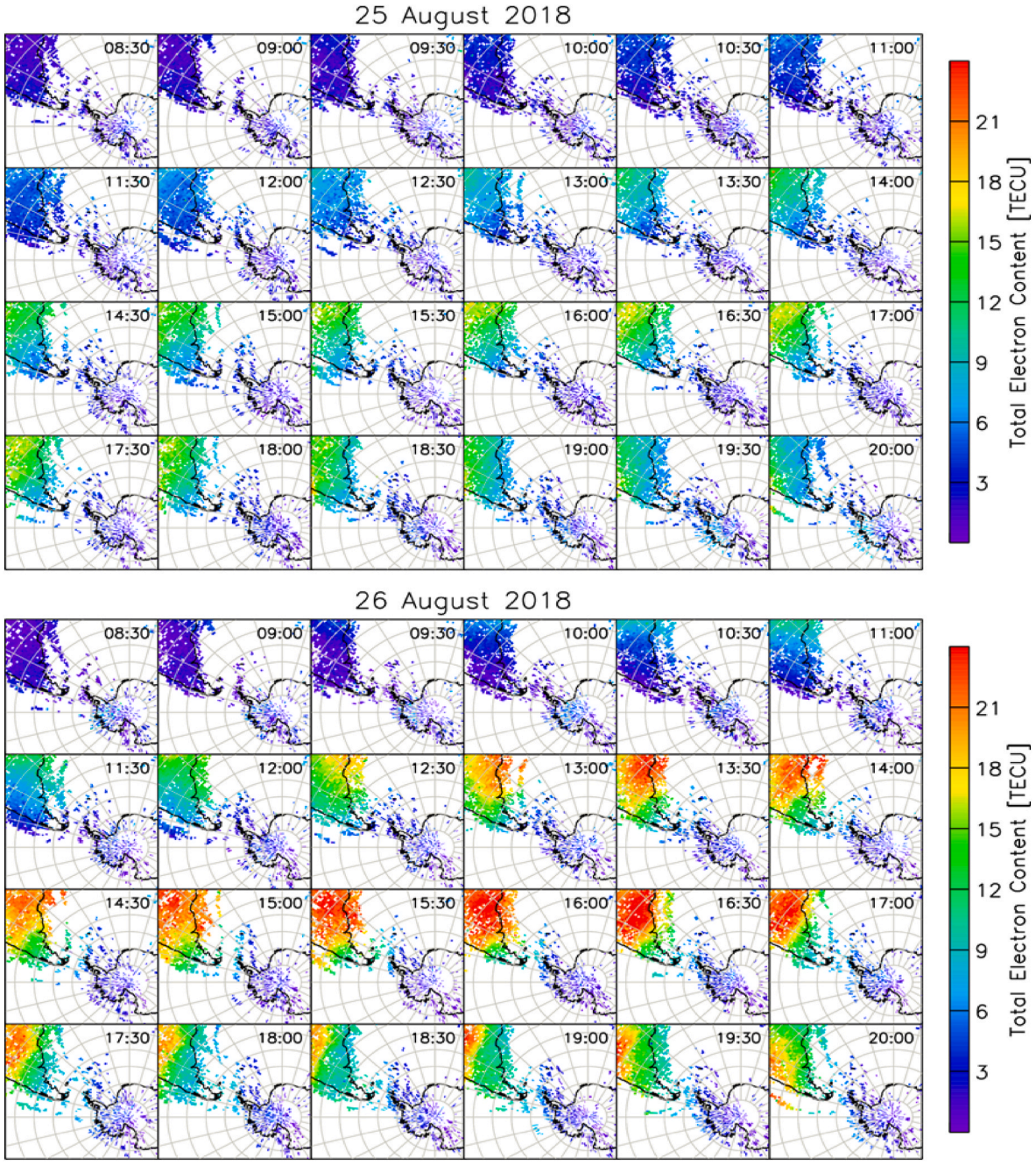

Fig. 8. Madrigal GPS-TEC maps over the South American and Antarctic sectors with contributions from nearly 200 GPS stations. The maps are from 25 to August 28, 2018 at 0830 to 2000 UT.

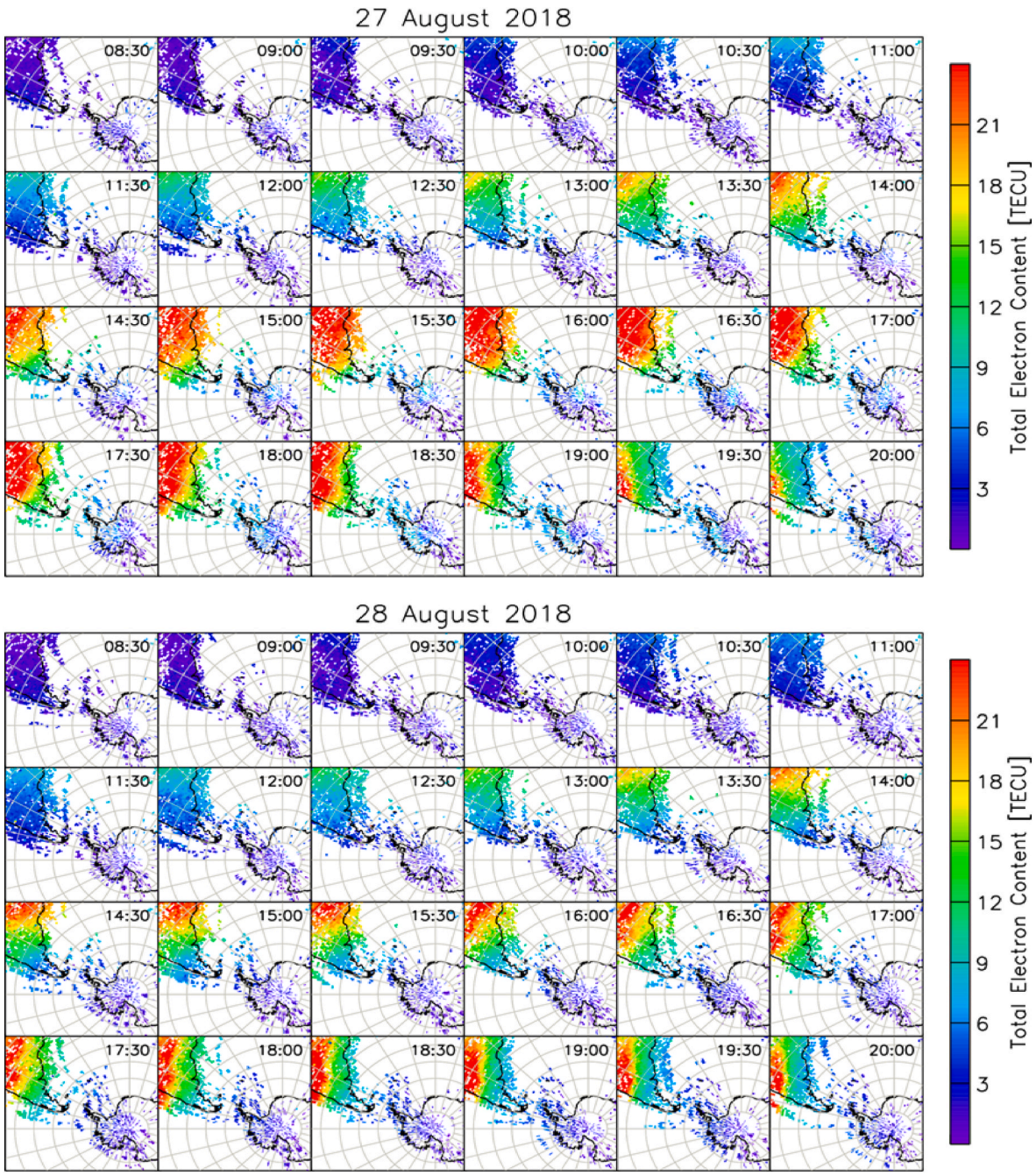

Fig. 8. (*continued*).

Prolss, 1995, 1997; Huang, 2013). However, as each mechanism generates ionospheric storm effects there are still open questions due to the complexity and dynamics of the ionospheric F region. The F region responds in different ways with respect to latitude and longitude in relation to the characteristics of each geomagnetic storm; for example, intensity (nT) and onsettime (LT) (Shahzad et al., 2023).

4.1. *Understanding TEC variability during main phase of the geomagnetic storm*

To identify how electric fields can develop and affect the ionosphere, we have to consider the results in Fig. 2. The long southward IMF-Bz can create conditions for undershielding electric fields and the resulting enhanced electric field causes eastward PPEF in dayside ionosphere. Fig. 9 shows the occurrence of eastward PPEF from 25 to August 27, 2018. The black line indicates quiet period plus penetration and the red line indicates only penetration. It is possible to observe in our investigation that during the main phase, eastward PPEF occurred. However, no significant ionospheric storm responses are observed. This eastward PPEF did not create conditions to alter the ionospheric plasma, as observed in the VTEC values (Fig. 3). Two factors can be considered for this: 1) slow decrease in Dst; and 2) local time of occurrence of PPEF. Our results show a slow decrease in Dst of the order of −11 nT/h and the main phase occurred at nighttime in this sector, so a low response from the ionospheric F region is to be expected. For the slow decrease in Dst, Wygant et al. (1998), using double-probe electric field experiment and the Air Force Geophysics Laboratory fluxgate magnetometer, investigated the PPEF during a major geomagnetic storm that occurred on March 24, 1991. Their investigation showed that during the decrease in Dst of the order of −15 nT/h, electric fields of weaker magnitude are

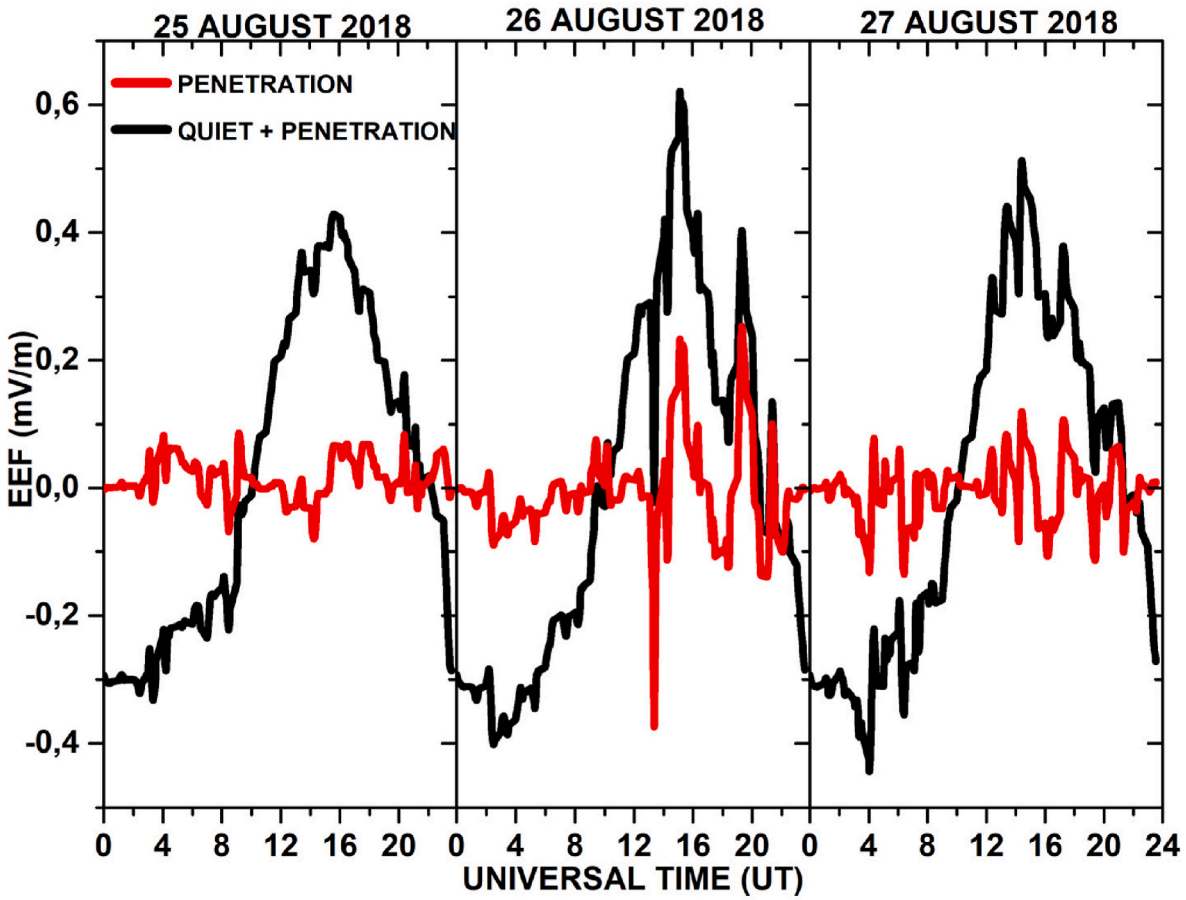

Fig. 9. Prompt penetration of electric field from 25 to August 27, 2018. The black line indicates quiet plus penetration and the red line indicates penetration only.

present. On the other hand, during the period of strong ring current growth rate, Dst decreases by −50 nT/h and stronger electric fields are observed. This study is also supported by (e.g., Basu et al., 2001; de Abreu et al., 2022). Basu et al. (2001) investigated two geomagnetic storms that occurred on 22–23 September and October 22, 1999, using GPS-TEC and satellite data. They observed a rapid decrease in Dst of about −50 nT/h associated with the occurrence of PPEF causing the largest effects on TEC values. de Abreu et al. (2022), using GPS-TEC and magnetometer observations, analyzed the ionospheric F region from the equator to the equatorial ionization anomaly regions over the South American sector during an intense geomagnetic storm of May 2017. Their results showed a slow decrease in Dst of about −20 nT/h and no effect of PPEF on TEC values during the main phase of the storm. Considering the nighttime occurrence of PPEF, Lissa et al. (2022), using GPS-TEC observations in the Indian equatorial and low-latitude sectors, investigated the storm of March 6, 2016. They also identified no changes in VTEC during the main phase that occurred at nighttime, due to the weak background electron density. The results obtained by TIE-GCM in this study also show low VTEC values, but with values below the observations.

4.2. Understanding TEC variability during recovery phase of the geomagnetic storm

During the recovery phase of the storm, our investigation shows a predominance of positive ionospheric storms, with large effects in VTEC values. This suggests that the cause for the positive phase observed in the recovery phase is possibly associated with the effects of electric fields and neutral winds. During the recovery phase, on 26 August, IMF-Bz shows three intense fluctuations between southward and northward directions. The strongest negative peaks (southward) occur around 1145 and 1500 UT and a third weaker one after 2030 UT. Consequently, the two positive peaks (northward) occur around 1330 and 1900 UT (Fig. 2). The eastward PPEF shows similar behavior to the IMF-Bz, but in the opposite direction, as can be seen in Fig. 9. As pointed out by Wei et al. (2008), PPEF can be classified into “single penetration” and “multiple penetration”, which are caused by an abrupt reversal and oscillations between northward and southward directions, respectively (see Table 1).

This can be better understood by analyzing the VTEC values in Fig. 3. Fig. 3 shows VTEC increases during the periods that IMF-Bz is southward during daytime, which means the presence of an eastward PPEF. VTEC increases due to the movement of charged particles in the ionosphere through the intensification of the **E** x **B** drift by PPEF. When the inversion occurs, a drop in VTEC values is observed. Table 2 shows the peak values of IMF-Bz (positive/negative meaning north/south direction) and PPEF (positive/negative meaning eastward/westward direction), and ionospheric storm (VTEC observations) on August 26, 2018, during recovery phase. Therefore, our results show an unusual case of multiple PPEF that occurred during the recovery phase in the South American and Antarctic sectors. Regarding the TIE-GCM model, it estimates the VTEC values during the storm, however, the variations in VTEC values due to the case of multiple PPEF, are not yet possible to estimate.

The long recovery phase continues to generate strong ionospheric storm effects from the near high-latitudes to the equatorial region. The day 27 continues to show a strong positive phase in all stations (Fig. 3). However, we cannot say that these are effects of PPEF, as the variations in IMF-Bz and eastward electric field are not accentuated, as shown in Figs. 2 and 9, respectively. The IMF-Bz is oscillating around zero, without incursions to the south or north. It can also be observed in Fig. 2,

Table 1
– Details of the Global Positioning System (GPS) sites used in the present study.

Location	Station (Network)	Lat.	Long.	Dip Lat.	Local Time (LT)
Equatorial Region					
São Luís (Brazil)	SALU (RBMC)	02.30° S	44.60° W	02.84° S	UT – 3 h
Palmas (Brazil)	TOPL (RBMC)	10.20° S	48.20° W	07.86° S	UT – 3 h
Low-Latitudes					
Brasília (Brazil)	BRAZ (RBMC)	15.90° S	47.90° W	12.88° S	UT – 3 h
Lins (Brazil)	SPLI (RBMC)	21.65° S	49.73° W	15.32° S	UT – 3 h
Curitiba (Brazil)	UFPR (RBMC)	25.30° S	49.20° W	17.90° S	UT – 3 h
Mid-Latitudes					
Colonia Del Sacramento (Uruguay)	UYCO (RAMSAC)	34.46° S	57.83° W	20.92° S	UT – 3 h
General Conesa (Argentina)	NESA (RAMSAC)	40.10° S	64.45° W	22.95° S	UT – 3 h
Esquel (Argentina)	ESQU (RAMSAC)	42.92° S	71.31° W	24.31° S	UT – 3 h
Ushuaia (Argentina)	AUTF (RAMSAC)	54.84° S	68.30° W	31.20° S	UT – 5 h
Near High-Latitudes					
O'Higgins (Antarctica)	OHI2 (IGS)	63.32° S	57.90° W	36.66° S	UT – 5 h

Table 2
– The August 26, 2018 recovery phase peak values of IMF-Bz (positive/negative meaning north/south direction) and PPEF (positive/negative meaning eastward/westward direction), and respective observed I onospheric storm (VTEC).

Time (UT)	IMF-Bz Peak (nT)	PPEF Peak (mV/m)	VTEC Observations 10 Stations
~1145	~-15	~+0.1	↑increase
~1330	~+16	~-0.4	↓drop
~1500	~-15	~+0.25	↑increase
~1900	~+12	~-0.1	↓drop
~2030	~-10	~+0.3	↑increase

a strong activity of the PCN and PCS indices above 7 mV/m. This is indicative of particle precipitation in the auroral region at both hemispheres. The global circulation of thermospheric winds changes significantly due to the Joule heating generated by particle precipitation and this can provide conditions for DDEF effects (Blanc and Richmond, 1980). During the daytime, the DDEF is westward, while at nighttime it is eastward. Thus, during the DDEF effects in the daytime, the eastward quiet zonal electric field should be weaker causing a decrease or suppression of the **E** x **B** drift (Yeeram, 2019). Therefore, we could expect a lower VTEC value, especially in the equatorial region, but our results do not show this. Fig. 3 shows high VTEC values from the equatorial region to near high-latitudes. This indicates that the positive phase observed on day 27 is possibly the effect of thermospheric wind disturbances. This is confirmed by Spogli et al. (2021), who, looking at the variations of foF2, revealed the occurrence of a positive phase due to thermospheric winds. On subsequent days of the storm (28, 29, and 30), there is still a positive phase, however, with less intensity, indicating the recovery of VTEC values to quiet conditions. On the other hand, it can be said that the TIE-GCM estimates the VTEC observations on 27 August, but with longer periods of positive phase from the equatorial region to the low-latitudes. From the mid-to near high-latitudes, the model underestimates the VTEC values. The following days, the model also underestimates VTEC observations.

Positive phase effects during the storm recovery phase have been studied by several researchers at different latitude and longitude sectors using different techniques (Balan et al., 2009; de Abreu et al., 2011; de Jesus et al., 2012; Habyarimana et al., 2023; and references therein). Balan et al. (2009), using observations and modeling, studied the importance of eastward PPEF and equatorward neutral wind in leading to positive ionospheric storms. They indicated that the equatorward wind can result in stronger positive phase. de Abreu et al. (2011) used GPS-TEC and ionosonde data to study a positive ionospheric storm phase over the Brazilian sector during the recovery phase of the super geomagnetic storm of May 2005. The observed effects are possibly due to the actions of equatorward winds. Habyarimana et al. (2023) used GPS-TEC to study the mechanisms that caused the effects during two geomagnetic storms that occurred on March 17, 2013 and 2015 over the East African sector. The positive phase observed may be due to strong disturbed dynamo electric field (DDEF), which was eastward during the night.

On the other hand, Huang (2019) analyzed ionospheric data measured by five Defense Meteorological Satellite Program satellites in the dusk-evening sector during the magnetic storm that occurred on 14–16 December 2006. They showed a peculiar feature: the vertical ion drift was enhanced in the upward directions by up to 180 m/s, corresponding to the occurrence of an eastward penetration electric field in the equatorial ionosphere, for 3 h in the storm main phase and 11 h in the recovery phase. This indicates that this storm presented different characteristics from the others studied (Manoj and Maus, 2012; Liu et al., 2018; and references therein).

In order to better understand the effects of the positive phase, we analyze the changes in thermospheric composition. Fig. 10 shows the global maps of the O/N_2 ratio from the CTIPe model for the period from 25 to August 28, 2018 at 0000 to 2000 UT each day. The value of the O/N_2 ratio increases during the recovery phase of the storm in near high-latitudes to equatorial region. The increase in the O/N_2 ratio results from a decrease of N_2. The N_2 is the main recombination product at altitudes in the ionospheric F region. However, during periods of storms where particle precipitation occurs at high-latitudes, the atomic oxygen O, being lighter than N_2, quickly reaches low-latitudes pushed by thermospheric winds through geomagnetic field lines, forming a positive phase (Zhang et al., 2014). This explains how thermospheric winds change the atmospheric composition, impacting the electron density. In order to support the results obtained by the model, Fig. 11 shows the global maps of the O/N_2 ratio obtained from the Global Ultraviolet Imager (GUVI) for the period 25 to August 30, 2018. An increase in the O/N_2 ratio can be observed during the recovery phase, in agreement with the model data. Therefore, it can be said that the positive phases observed during the recovery phase period are possibly due to the effects of electric fields (26 August) and neutral winds (27 August) causing increases in thermospheric composition.

5. Conclusion

In this paper, we have presented GPS-VTEC observations and their comparison with the TIE-GCM model output to study the response of the ionospheric F region in the South American and Antarctic sectors during the intense geomagnetic storm of 25–27 August 2018. Main features associated with these observations are summarized below.

During the main phase of the storm, a southward IMF-Bz is observed, which was accompanied by an eastward PPEF that did not significantly impact the ionospheric plasma. This was possibly related to the slow decrease in Dst on the order of −11 nT/h and the main phase that occurred at nighttime.

A long recovery phase is observed with a predominance of positive phase during daytime. On the first day of the recovery phase, 26 August, the observations showed an unusual case of multiple PPEF, which affected the VTEC values. The next day, 27 August, the observations possibly showed effects of thermospheric wind disturbances in the VTEC values.

Considering the comparison of the TIE-GCM model with the GPS-VTEC observations, it can be concluded that the model reproduces the

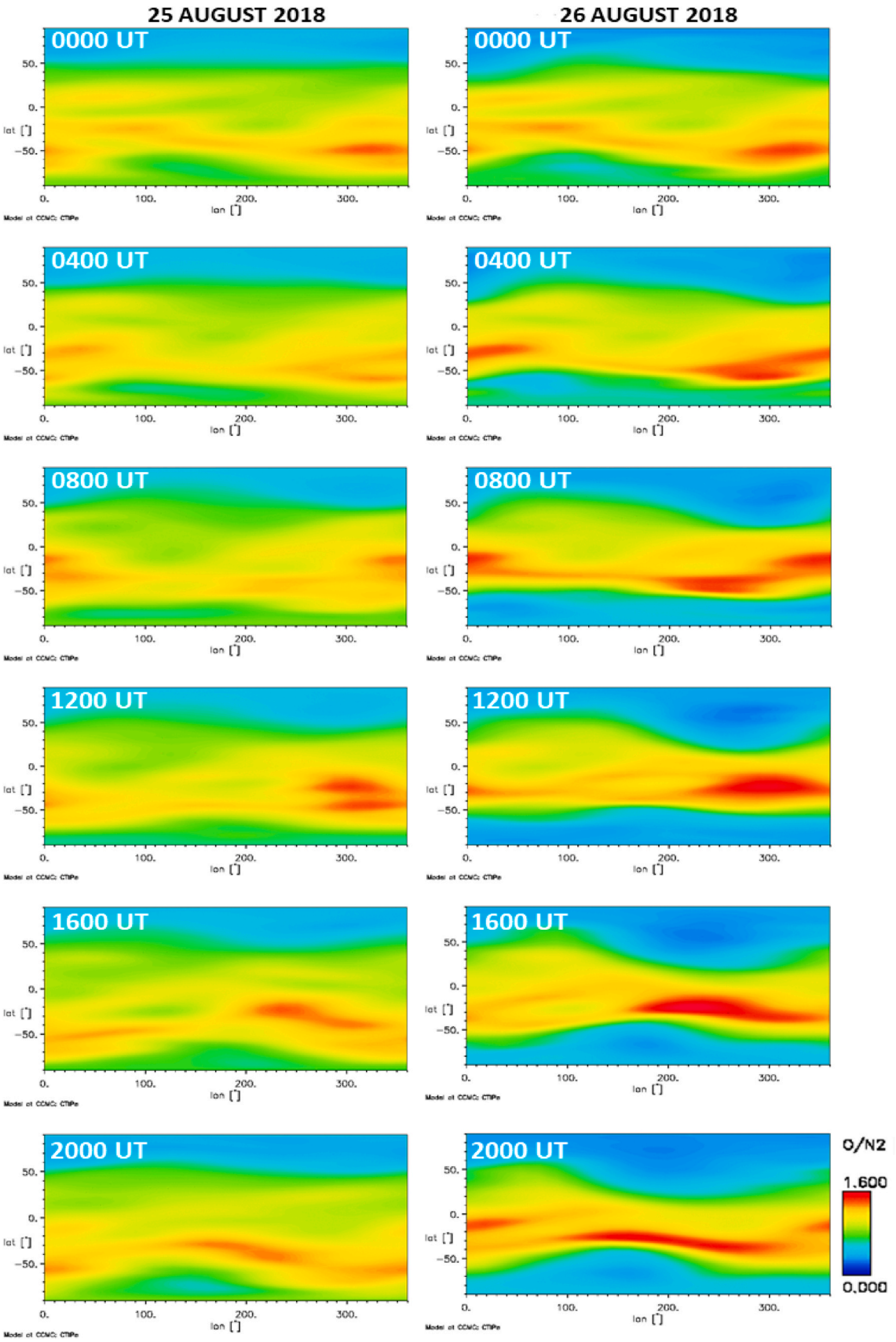

Fig. 10. Global maps of the O/N_2 ratio from the CTIPe model for the period from 25 to August 28, 2018 at 0000 to 2000 UT.

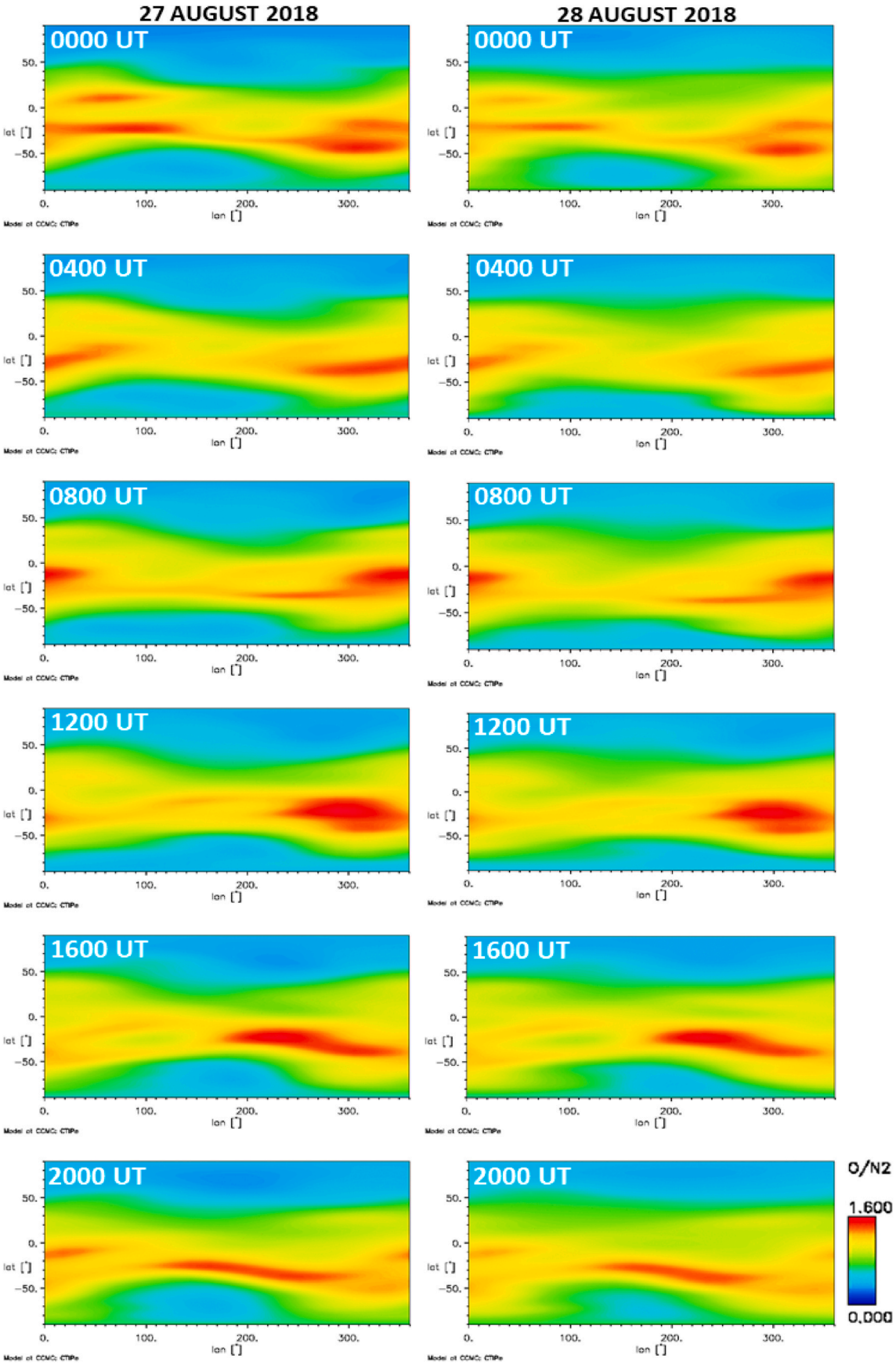

Fig. 10. (*continued*).

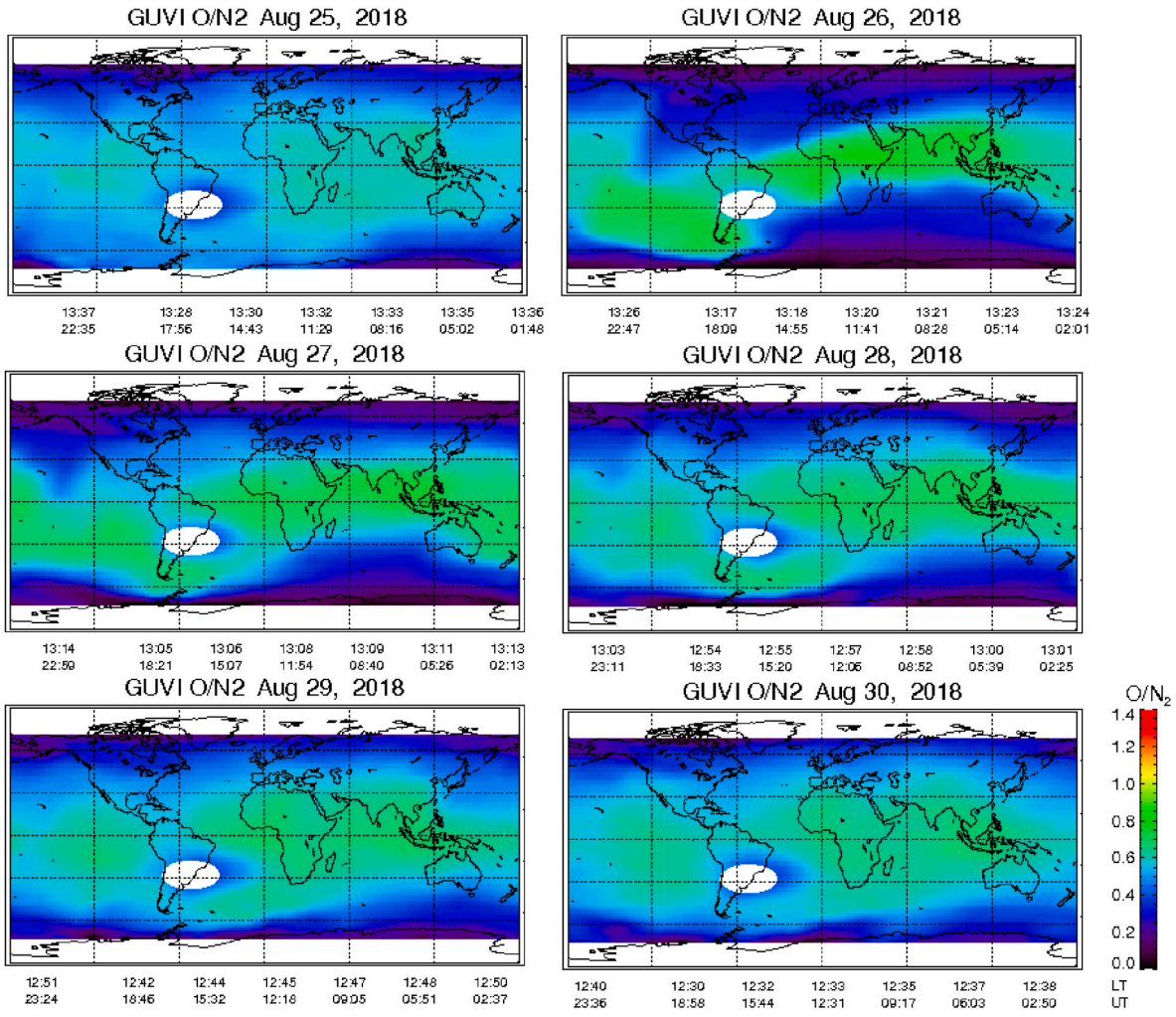

Fig. 11. Global maps of the O/N_2 ratio from the Global Time Series Gallery for the period from 25 to August 30, 2018.

VTEC increases during the main and recovery phases at mid-latitudes up to the equatorial region. However, the variations in VTEC values due to the case of multiple PPEF is not captured by the model. Also, near high-latitudes, the model underestimates the observations.

Finally, this study showed that the positive phase observed during the recovery phase of the storm due to the penetrating effects of electric fields and winds caused an increase in thermospheric composition. Therefore, we suggest that more analysis will be necessary for a complete understanding, especially when it comes to PPEF.

CRediT authorship contribution statement

A.J. de Abreu: Writing – original draft, Resources, Investigation, Conceptualization. **E. Correia:** Supervision. **O.F. Jonah:** Methodology. **K. Venkatesh:** Software. **E.G. Thomas:** Software. **R. de Jesus:** Data curation. **M. Roberto:** Resources. **J.R. Abalde:** Resources. **P.R. Fagundes:** Resources.

Declaration of competing interest

The authors declare that they have no known competing financial interests or personal relationships that could have appeared to influence the work reported in this paper.

Acknowledgements

The authors thank the authorities of the “Rede Brasileira de Monitoramento Contínuo de GPS (RBMC)”, Brazil; “Red Argentina de Monitoreo Satelital Continuo (RAMSAC)”; and International Global Navigation Satellite System (GNSS) Service (IGS), for kindly allowing us to use the data. Also, O/N_2 ratio data (https://guvitimed.jhuapl.edu/guvi-galleryl3on2). K.V. acknowledge Department of Space, Govt. of India for the support. R.J acknowledges the CNPq, grants 317447/2023-8 and 300229/2024-0, for providing fellowship. E.G.T. acknowledges support from the National Science Foundation under grant AGS-1934997. The authors also thank the Brazilian funding agency “CNPq” for kindly providing the partial financial support.

Data availability

The authors do not have permission to share data.

References

Akala, A.O., Oyedokun, O.J., Amaechi, P.O., Simi, K.G., Ogwala, A., Arowolo, O.A., 2021. Solar origins of August 26, 2018 geomagnetic storm: responses of the interplanetary medium and equatorial/low-latitude ionosphere to the storm. Space Weather 19, e2021SW002734. https://doi.org/10.1029/2021SW002734.

Akasofu, S.-I., 1981. Prediction of development of geomagnetic storms using the solar wind- magnetosphere energy coupling function [epsi]. Planet. Space Sci. 29 (11), 1151–1158.

Balan, N., Alleyne, H., Otsuka, Y., Lekshmi, D.V., Fejer, B.G., McCrea, I., 2009. Relative effects of electric field and neutral wind on positive ionospheric storms. Earth Planets Space 61, 439–445.
Blanc, M., Richmond, A.D., 1980. The ionospheric disturbance dynamo. J. Geophys. Res. 85 (A4), 1669–1686. https://doi.org/10.1029/JA085iA04p01669.
Boteler, D.H., Pirjola, R.J., Nevanlinna, H., 1998. The effects of geomagnetic disturbances on electrical systems at the Earth's surface. Adv. Space Res. 22 (1), 17–27.
Basu, S., Basu, Su, Valladares, C.E., Yeh, H.-C., Su, S.-Y., Mackenzie, E., Sultan, P.J., Aarons, J., Rich, F.J., Doherty, P., Groves, K.M., Bullet, T.W., 2001. Ionospheric effects of major magnetic stormsduring the international space weather period of September and October 1999: GPS observations, VHF/UHF scintillations, and in situ density structures at middle and equatorial latitudes. J. Geophys. Res. 106 (A12), 30,389–30,413.
Buonsanto, M.J., 1999. Ionospheric storms – a review. Space Sci. Rev. 88, 563–601.
Chen, C., Liu, Y.D., Wang, R., Zhao, X., Hu, H., Zhu, B., 2019. Characteristics of a gradual filament eruption and subsequent CME propagation in relation to a strong geomagnetic storm. Astrophys. J. 884 (1), 90.
Chingarandi, F.S., Candido, C.M.N., Becker-Guedes, F., Jonah, O.F., Moraes-Santos, S.P., Klausner, V., Taiwo, O.O., 2023. Assessing the effects of a minor CIR-HSS geomagnetic storm on the Brazilian low-latitude ionosphere: ground and space-based observations. Space Weather 21 (9).
Danilov, A.D., Morozova, L.D., 1985. Ionospheric storms in the F2 region: morphology and physics. Geomagn. Aeron. 25, 593–605 submitted for publication.
de Abreu, A.J., Sahai, Y., Fagundes, P.R., de Jesus, R., Bittencourt, J.A., Pillat, V.G., 2011. An investigation of ionospheric F region response in the Brazilian sector to the super geomagnetic storm of May 2005. Adv. Space Res. 48, 1211–1220.
de Abreu, A.J., Martin, I.M., Fagundes, P.R., Venkatesh, K., Batista, I.S., de Jesus, R., Rockenback, M., Coster, A., Gende, M., Alves, M.A., Wild, M., 2017. Ionospheric F-region observations over American sector during an intense space weather event using multi-instruments. J. Atmos. Sol. Terr. Phys. 156, 1–14.
de Abreu, A.J., Correia, E., Denardini, C.M., de Jesus, R., Venkatesh, K., Roberto, M., Abalde, J.R., Fagundes, P.R., Bolzan, M.J.A., Gende, M., 2022. Ionospheric GPS-TEC respondes from equatorial regions to the EIA crest in the South American sector under intense space weather conditions. J. Atmos. Sol. Terr. Phys. 105801.
de Abreu, A.J., Correia, E., de Jesus, R., Venkatesh, K., Macho, E.P., Roberto, M., Fagundes, P.R., Gende, M., 2023. Statistical analysis on the ionospheric response over South American mid-and near high-latitudes during 70 intense geomagnetic storms occurred in the period of two decades. J. Atmos. Sol. Terr. Phys. 245, 106060. https://doi.org/10.1016/j.jastp.2023.106060.
de Jesus, R., Sahai, Y., Guarnieri, F.L., Fagundes, P.R., de Abreu, A.J., Bittencourt, J.A., Nagatsuma, T., Huang, C.S., Lan, H.T., Pillat, V.G., 2012. Ionospheric response of equatorial and low latitude F-region during the intense geomagnetic storm on 24–25 August 2005. Adv. Space Res. 49 (3), 518–529. https://doi.org/10.1016/j.asr.2011.10.020.
de Jesus, R., Sahai, Y., Fagundes, P.R., de Abreu, A.J., Brunini, C., Gende, M., Bittencourt, J.A., Abalde, J.R., Pillat, V.G., 2013. Response of equatorial, low- and mid- latitude F-region in the American sector during the intense geomagnetic storm on 24 - 25 October 2011. Adv. Space Res. 147–157.
Fagundes, P.R., Tasil Brown, V.Y., Pillat, V.G., arcanjo, M.O., Venkatesh, K., Habarulema, J.B., Bolzan, M.J.A., de Jesus, R., de Abreu, A.J., Tardelli, A., Vieira, F., Denardini, C.M., 2023. Ionospheric storm due to solar Coronal mass ejection in September 2017 over the Brazilian and African longitudes. Adv. Space Res. 71 (1), 46–66. https://doi.org/10.1016/j.asr.2022.07.040.
Foster, J.C., Rideout, W., 2005. Midlatitude TEC enhancements during the October 2003 superstorm: observations, storm dynamics, and relative importance of the fountain effect. J. Geophys. Res.: Space Phys. 110 (A9), A09S31. https://doi.org/10.1029/2004JA010928.
Fuller-Rowell, T.J., Rees, D., Quegan, S., Moffett, R.J., Bailey, G.J., 1987. Interactions between neutral thermospheric composition and the polar ionosphere using a coupled ionosphere-thermosphere model. J. Geophys. Res. 92, 7744. https://doi.org/10.1029/ja092ia07p07744.
Fuller-Rowell, T.J., Codrescu, M.V., Moffett, R.J., Quegan, S., 1996. Response of the thermosphere and ionosphere to geomagnetic storms. J. Geophys. Res.: Space Phys. 101 (A2), 2343–2353. https://doi.org/10.1029/95JA02015.
Gonzalez, W.D., Gonzalez, A.L.C., Tsurutani, B.T., 1990. Dual-peak solar cycle distribution of intense geomagnetic storms. Planet. Space Sci. 38, 181.
Habyarimana, V., Habarulema, J.B., Dugassa, T., 2023. Analysis of ionospheric storm-time effects over the East African sector during the 17 March 2013 and 2015 geomagnetic storms. Earth Planets Space 75 (58).
Huang, C.M., 2013. Disturbance dynamo electric fields in response to geomagnetic storms occurring at different universal times. J. Geophys. Res. 118, 496–501. https://doi.org/10.1029/2012JA018118.
Huang, C.M., 2019. Long-Lasting penetration electric fields during geomagnetic storms: observations and mechanisms. J. Geophys. Res. 2019.
Jonah, Olusegun F., Zhang, Shunrong, Coster, Anthea J., Goncharenko, Larisa P., Erickson, Philip J., Rideout, William, De Paula, Eurico R., de Jesus, Rodolfo, 2020. Understanding inter-hemispheric traveling ionospheric disturbances and their mechanisms. Rem. Sens. 12, 228.
Kikuchi, T., Hashimoto, K.K., Tanaka, T., Nishimura, Y., Nagatsuma, T., 2022. Middle latitude geomagnetic disturbances caused by Hall and pedersen current circuits driven by prompt penetration electric fields. Atmosphere 13, 580. https://doi.org/10.3390/atmos13040580.
Klimenko, M.V., Klimenko, V.V., Ratovsky, K.G., Goncharenko, L.P., Sahai, Y., Fagundes, P.R., de Jesus, R., de Abreu, A.J., Vesnin, A.M., 2011. Numerical modeling of ionospheric effects in the middle- and low-latitude *F* region during geomagnetic storm sequence of 9 14 September 2005. Radio Sci. 46, RS0D03.
Klobuchar, J.A., 1996. Ionospheric effects on GPS. In: Parkinson, B.W., Spilker, J.J. (Eds.), Global Positioning System: Theory and Applications, vol. 2, p. 485. Progress in Astronautics and Aeronautics, 164.
Laundal, K.M., Richmond, A.D., 2016. Magnetic coordinate systems. Space Sci. Rev. https://doi.org/10.1007/s11214-016-0275-y.
Lissa, D., Venkatesh, K., Prasad, D.S.V.V.D., Niranjan, K., 2022. Distinct ionospheric response to three different geomagnetic storms during 2016 using GPS-TEC observations over the Indian equatorial and low latitude sectors. Adv. Space Res. 70 (4), 1089–1103.
Liu, Y., Fu, L., Wang, J., Zhang, C., 2018. Studying ionosphere responses to a geomagnetic storm in June 2015 with multi-constellation observations. Rem. Sens. 10, 666.
Manoj, C., Maus, S., 2012. A real-time forecast service for the ionospheric equatorial zonal electric field. Space Weather 10, S09002.
Mansilla, G.A., Zossi, M.M., 2022. Ionospheric response to the 26 August 2018 geomagnetic storm along 280° E and 316° E in the South American sector. Adv. Space Res. 69 (Issue 1), 48–58.
Maruyama, N., Richmond, A.D., Fuller-Rowell, T.J., Codrescu, M.V., Sazykin, S., Toffoletto, F.R., Spiro, R.W., Millward, G.H., 2005. Interaction between direct penetration and disturbance dynamo electric fields in the storm-time equatorial ionosphere. J. Geophysical Research 32, L17105. https://doi.org/10.1029/2005GL023763.
Pandit, D., Ghimire, B., Amory-Mazaudier, C., Fleury, R., Chapagain, N.P., Adhikari, B., 2021. Climatology of ionosphere over Nepal based on GPS total electron content data from 2008 to 2018. Ann. Geophys. 39, 743–758. https://doi.org/10.5194/angeo-39-743-2021.
Prölss, G.W., 1993. On explaining the local time variation of ionospheric storm effects. Ann. Geophys. 11, 1–9.
Prolss, G.W., 1995. Ionospheric F-region storms. In: Handbook of Atmospheric Electrodynamics, vol. II.
Prolss, G.W., 1997. Magnetic storm associated perturbations of the Upper atmo- sphere. In: Tsurutani, B.T., et al. (Eds.), Magnetic Storms, Geophys. Monogr. Ser, vol. 98. AGU, Washington, DC, pp. 227–241.
Ren, D., Lei, J., Zhou, S., Li, W., Huang, F., Luan, X., et al., 2020. High-speed solar wind imprints on the ionosphere during the recovery phase of the August 2018 geomagnetic storm. Space Weather 18, e2020SW002480. https://doi.org/10.1029/2020SW002480.
Richmond, A.D., Kamide, Y., 1988. Mapping electrodynamic features of the high-latitude ionosphere. J. Geophys. Res.: Space Phys. 93 (A6), 5741–5759. https://doi.org/10.1029/JA093iA06p05741.
Richmond, A.D., Lu, G., 2000. Upper-atmospheric effects of magnetic storms: a brief review. J. Atmos. Sol. Terr. Phys. 62 (12), 1115–1127. https://doi.org/10.1016/S1364-6826(00)00094-8.
Rideout, W., Coster, A., 2006. Automated GPS processing for global total electron content data. GPS Solut. 10 (3), 219–228.
Roble, R.G., Ridley, E.C., 1987. An auroral model for the NCAR thermospheric general circulation model (TGCM). Annales Geophys 5A, 369–382.
Sahai, Y., Becker-Guedes, F., Fagundes, P.R., Lima, W.L.C., de Abreu, A.J., Guarnieri, F. L., Candido, C.M.N., Pillat, V., 2007. Unusual ionospheric effects observed during the intense 28 October 2003 solar flare in the Brazilian sector. Ann. Geophys. 25, 2497–2502.
Seemala, G.K., Valladeres, C.E., 2011. Statistics of total electron content depletions observed over the South American continent for the year 2008. Radio Sci. 46, RS5019. https://doi.org/10.1029/2011RS004722.
Shahzad, R., Shah, M., Tariq, M.A., Calabia, A., Melgarejo-Morales, A., Jamjareegulgarn, P., Liu, L., 2023. Ionospheric–thermospheric responses to geomagnetic storms from multi-instrument space weather data. Rem. Sens. 15, 2687. https://doi.org/10.3390/rs15102687.
Spogli, L., Sabbagh, D., Regi, M., Cesaroni, C., Perrone, L., Alfonsi, L., et al., 2021. Ionospheric response over Brazil to the August 2018 geomagnetic storm as probed by CSES-01 and Swarm satellites and by local groundbased observations. J. Geophys. Res.: Space Phys. 126, e2020JA028368. https://doi.org/10.1029/2020JA028368.
Veenadhari, B., Alex, S., Kikuchi, T., Shinbori, A., Singh, R., Chandrasekhar, E., 2010. Penetration of magnetospheric electric fields to the equator and their effects on the low-latitude ionosphere during intense geomagnetic storms. J. Geophys. Res. 115, A03305. https://doi.org/10.1029/2009JA014562.
Venkatesh, K., Tulasi Ram, S., Fagundes, P.R., Seemala, Gopi K., Batista, I.S., 2017. Electrodynamic disturbances in the Brazilian equatorial and low-latitude ionosphere on St. Patrick's Day storm of 17 March 2015. J. Geophys. Res. Space Physics 122, 4553–4570. https://doi.org/10.1002/2017JA024009.
Vierinen, J., Coster, A.J., Rideout, W.C., Erickson, P.J., Norberg, J., 2016. Statistical framework for estimating GNSS bias. Atmos. Meas. Tech. 9, 1303–1312. https://doi.org/10.5194/amt-9-1303-2016.
Wei, Y., Hong, M., Wan, W., Du, A., Lei, J., Zhao, B., Wang, W., Ren, Z., Yue, X., 2008. Unusually long lasting multiple penetration of interplanetary electric field to equatorial ionosphere under oscillating IMF Bz. Geophys. Res. Lett. 35, L02102. https://doi.org/10.1029/2007GL032305.
Willis, D.M., 1964. The sudden commencement and first phase of a geomagnetic storm. J. Atmos. Terr. Phys. 26 (5), 581–602.
Wygant, J., Rowland, D., Singer, H.J., Temerin, M., Mozer, F., Hudson, M.K., 1998. Experimental evidence on the role of the large spatial scale electric field in creating the ring current. J. Geophys. Res. 103, 29527–29544. https://doi.org/10.1029/98JA01436.

Yeeram, T., 2019. The solar wind-magnetosphere coupling and daytime disturbance electric fields in equatorial ionosphere during consecutive recurrent geomagnetic storms. J. Atmos. Sol. Terr. Phys. 187, 40–52.

Waqar, Younas, Amory-mazaudier, C., Majid, Khan, Le Huy, M., 2021. Magnetic signatures of ionospheric disturbance dynamo for CME and HSSWs generated storms. Space Weather 19 (9). https://dx.doi.org/10.1029/2021SW002825.

Zhang, Y., Paxton, L.J., Morrison, D., Marsh, D., Kil, H., 2014. Storm-time behaviors of O/N2 and NO variations. J. Atmos. Sol. Terr. Phys. 114, 42–49.

Zolotukhina, N., Polekh, N., Kurkin, V., Rogov, D., Romanova, E., Chelpanov, M., 2017. Ionospheric effects of st. Patrick's storm over asian Russia: 17–19 March 2015. J. Geophys. Res. Space Physics 122 (2), 2484–2504. https://doi.org/10.1002/2016JA023180.

Zou, Y., Wang, W., Zhang, Y., Luhr, H., 2014. The ionospheric response to high-latitude forcing during 17–18 March 2013 storm: impact of neutral winds and electrodynamic coupling. J. Geophys. Res.: Space Phys. 119 (9), 7967–7979. https://doi.org/10.1002/2014JA019891.